Control Engineering Practice 85 (2019) 206–215

Contents lists available at ScienceDirect

Control Engineering Practice

journal homepage: www.elsevier.com/locate/conengprac

Model-based temperature estimation of power electronics systems

Pamela J. Tannous [a], Satya R.T. Peddada [b], James T. Allison [b], Thomas Foulkes [c], Robert C.N. Pilawa-Podgurski [c], Andrew G. Alleyne [a,*]

[a] Mechanical Science and Engineering Department, University of Illinois at Urbana-Champaign, Urbana, IL 61801, USA
[b] Industrial and Enterprise Systems Engineering Department, University of Illinois at Urbana-Champaign, Urbana, IL 61801, USA
[c] Electrical and Computer Engineering Department, University of Illinois at Urbana-Champaign, Urbana, IL 61801, USA

ARTICLE INFO

Keywords:
Thermal modeling
Kalman filter
Structure-preserving model order reduction
Dynamic thermal estimation
Fault detection

ABSTRACT

This paper proposes a method for accurate temperature estimation of thermally-aware power electronics systems. The duality between electrical systems and thermal systems was considered for thermal modeling. High dimensional thermal models present a challenge for online estimation. Therefore, the complexity of the thermal network was reduced by applying a structure-preserving model order reduction technique. An optimal number and placement of temperature sensors were used in a Kalman filter to accurately estimate the dynamic spatial thermal behavior of the system. The optimal number of temperature sensors was found by comparing the actual values of the states obtained from the thermal model to the estimated values of the states obtained from the Kalman filter. The optimal placement of temperature sensors was found by maximizing the trace of the observability Gramian. Simulation and experimental results validate the approach on a prototype inverter.

1. Introduction

With the emerging trend of increasing the power density within power electronics comes the limitation of power dissipation in the system. This increase in power dissipation leads to an inevitable increase in temperature (Pedram & Nazarian, 2006) that has negative effects on the performance and lifetime of the components operating in the power electronic system. Also, higher temperature increases the cooling cost which is a major problem in the current power electronics field (Coskun, Rosing, & Whisnant, 2007; Davidson, Stone, Foster, & Gladwin, 2016; Huang, Ghosh, Velusamy, Sankaranarayanan, Skadron, & Stan, 2006; Iachello et al., 2014; Lim, Daasch, & Cai, 2002; Pedram & Nazarian, 2006; Zanini, Atienza, Jones, & De Micheli, 2010).

The objective of this research is to obtain an accurate estimate of the spatial dynamic thermal profile of thermally-aware power electronic systems using the smallest number of temperature sensors in the system. Dynamic thermal management (DTM) has been proven to be an effective solution to control the temperature by guaranteeing that the temperature of the hotspots in the power module will not violate a specific threshold. However, this technique typically relies on thermal measurements obtained from on-board sensors. Therefore, accurate temperature readings of the system are essential for a successful DTM approach (Sharifi & Rosing, 2010; Zhang & Srivastava, 2010; Zhang, Srivastava, & Zahran, 2008).

Power electronic systems that estimate their own temperature to apply thermal management techniques, possibly by reducing their power flow, are known by thermally-aware power electronics (Lim et al., 2002). Increasing the power density becomes safer in this new breed of power electronic systems since the availability of the accurate dynamic temperature profile in these systems activates the DTM at the right time. Accurate thermal readings can be obtained by increasing the number of sensors in the system. However, a large number of sensors influences the reliability and packaging of the system, increases its cost, and interferes with its circuit design (Sharifi & Rosing, 2010). Furthermore, the locations of the temperature sensors in the system affect the accuracy of the estimated parameters by interfering with the thermal transport that would occur in their absence.

Significant work has been done on the temperature estimation for a single chip (Sharifi & Rosing, 2010) but this benefits from homogeneous material and components, something lacking in a heterogeneous power module. Additionally, (Davidson et al., 2016) recently implemented a data-driven estimation scheme in the frequency domain for power electronics. The method proposed in this paper provides an accurate thermal estimation of highly complex and heterogeneous systems using an online model-driven estimator in the time domain coupled with structure-preserving compact thermal models. Early results for 2 dimensional (2D) planar systems were presented in Tannous (2017) and this work builds on it by extending to 3 dimensional (3D) systems with additional fault detection functionality.

The main contribution of this work is the development and experimental validation of an overall approach to accurately determine full

* Corresponding author.
E-mail addresses: tannous2@illinois.edu (P.J. Tannous), speddad2@illinois.edu (S.R.T. Peddada), jtalliso@illinois.edu (J.T. Allison), foulkes2@illinois.edu (T. Foulkes), pilawa@illinois.edu (R.C.N. Pilawa-Podgurski), alleyne@illinois.edu (A.G. Alleyne).

https://doi.org/10.1016/j.conengprac.2019.01.006
Received 6 November 2017; Received in revised form 8 November 2018; Accepted 9 January 2019
Available online xxxx
0967-0661/

thermal state with minimal sensing for power electronics using dynamic RC modeling of heterogeneous structures, structure-preserving model order reduction, hybrid Kalman filtering, and optimal number and placement of temperature sensors. The rest of this article is organized as follows. Section 2 describes the thermal network modeling procedure for 2D and 3D systems. Section 3 describes the model order reduction technique used to reduce the complexity of 2D and 3D systems. Section 4 describes the estimator design. Section 5 describes two case studies in which the proposed method was tested on an actual 2D multi-level inverter and an actual 3D multi-level inverter. Section 6 presents conclusions.

2. Thermal network modeling

The dynamic physical systems of interest have temporally and spatially varying temperature profiles. Detailed modeling of thermal interaction in these systems results in high dimensional complex models that are inappropriate for estimation and control design purposes. The appropriate modeling approach needs to balance complexity versus accuracy; by that it is meant that the thermal models should be simple enough for on-line implementation and detailed enough to simulate the dynamic thermal behavior of the systems at an acceptable level of accuracy. The number of powerful analysis tools drops significantly for non-linear systems compared to linear systems (Atherton, 1982) leading to a strong preference for linear models. Therefore, the physical systems analyzed were approximated using lumped parameter models by deriving an equivalent thermal circuit (Iachello & others, 2014). Collecting these models results in a directed connected graph of linear systems. Model order reduction techniques can be used to further reduce the dimension of the lumped parameter models and this idea is detailed in Section 3.

The first step towards getting an accurate temperature estimation of thermally-aware power electronic systems is to create a thermal model that provides a sufficiently accurate representation of the dynamic thermal behavior of the system. As shown in the literature, a resistor–capacitor (RC) thermal model can successfully simulate the spatial dynamic temperature distribution of the system with a reasonable accuracy and complexity tradeoff (Huang et al., 2006; Sharifi, Liu, & Rosing, 2008; Skadron, Abdelzaher, & Stan, 2002; Swift, Molinski, & Lehn, 2001; Zhang & Srivastava, 2010). This thermal network is created by considering the similarity between an electric circuit and a thermal circuit since current and heat flow are described with the same differential equations. This similarity converts the heat conduction problem into an electric problem where the voltage in the RC circuit represents the temperature, the current represents the heat transfer, and the electrical resistances represent the thermal resistances.

The heat conduction problem can be solved as a one dimensional (1D) problem, 2D problem, or 3D problem (Jena, Sarbhai, Mulaveesala, & Tuli, 2006). For a 1D heat conduction problem, the system is divided into blocks along just one direction. The blocks are connected to each other through a thermal resistance. For a 2D heat conduction problem, the system is considered as a plate that is divided into pixels with an assigned capacitor to each one of these elements and assigned resistors that connect each capacitor to one other in the x and y directions. For a 3D heat conduction problem, the system is divided into small cubes, or voxels, with assigned resistors and capacitors that account for the conduction along three dimensions. The 2D and 3D RC thermal models will be explained in more details in the next two subsections.

2.1. 2D RC thermal model

2D RC thermal models account for conduction along the x and y directions in the plane of the system in addition to the convective heat transfer from the system to the ambient atmosphere. The first step in designing a RC thermal model is to discretize the system into pixels. To reduce the complexity of the thermal model, the level of granularity chosen was at the level of the functional elements (Huang et al., 2006). Therefore, each functional block is represented by a single node and assigned a capacitor in the RC thermal model. The heat generated from the functional blocks is modeled as current sources connected to the corresponding capacitors in the RC model.

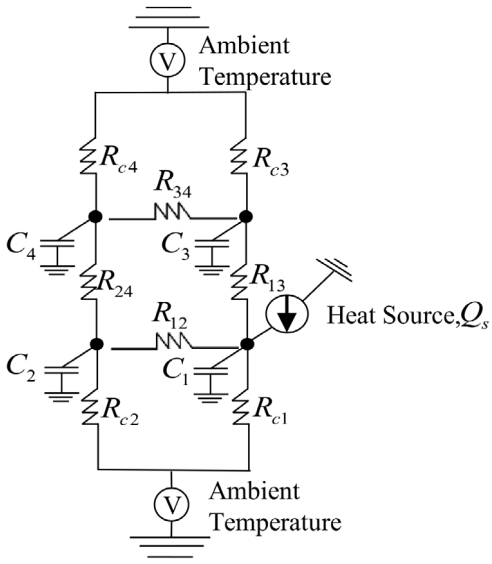

Fig. 1. Example of a 2-D RC thermal model of a system that was partitioned into 4 pixels.

The convective heat transfer from each functional block to the ambient atmosphere is represented in the RC model by a resistor that connects the relevant capacitor to the ambient temperature. The ambient temperature is represented in the RC model by a voltage source. Fig. 1 shows an example of a 2D RC circuit for a system divided into 4 elements. The heat generated in the first functional element was modeled by the current source connected to the first capacitor.

The next step in designing the RC thermal model is to compute the resistor and capacitor values. The conduction resistance is given by Frank, Incropera, DeWitt, and Bergman (2007)

$$R_{cond} = \frac{L}{KA_c}, \tag{1}$$

where L is the length through which the heat is being conducted, K is the thermal conductivity of the material, and A_c is the cross-sectional area through which the heat is being conducted. The type of heat transfer from a surface of a system depends on whether that surface is a free surface or a connected surface. A free surface experiences convective heat transfer to the ambient atmosphere. A connected surface experiences conductive heat transfer to the surface connected to it.

The convection resistance is given by Frank et al. (2007)

$$R_{conv} = \frac{1}{hA_s}, \tag{2}$$

where h is the convective heat transfer coefficient, and A_s is the surface area from which the heat is being lost to the ambient environment as shown in Fig. 2. The thermal capacitance is given by Frank et al. (2007)

$$C = \rho c V, \tag{3}$$

where ρ is the density of the material, c is the specific heat capacity of the material, and V is the volume of the corresponding element of the system.

If the system is composed of multiple layers of different materials, it is convenient to treat the multilayered structure as a homogeneous material with an in-plane effective thermal conductivity given by Frank et al. (2007)

$$K_{in-plane} = \frac{\sum_{i=1}^{N} K_i t_i}{\sum_{i=1}^{N} t_i}, \tag{4}$$

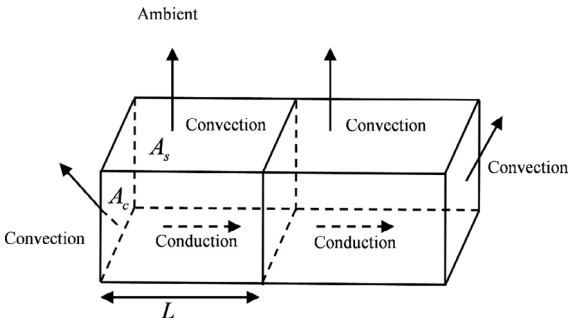

Fig. 2. Types of heat transfer from 2 functional blocks.

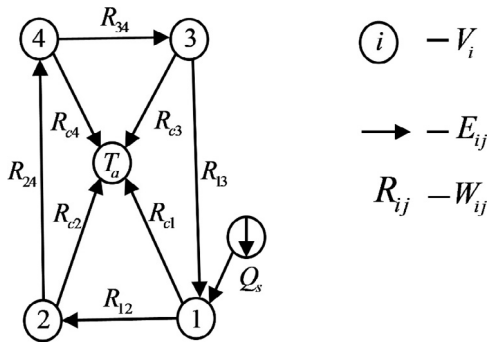

Fig. 3. Example of a 2D graph-based thermal model.

where K_i is the thermal conductivity of a specific layer, t_i is the thickness of the corresponding layer, and N is the total number of layers. The effective thermal capacitance of the multilayered structure is the sum of the thermal capacitance (3) of each layer (Frank et al., 2007)

$$C = \sum_{i=1}^{N} C_i. \tag{5}$$

2.2. 3D RC thermal model

Some power electronic systems are enclosed by heat sinks. In this case, there is no convective heat transfer between the components of the system and the ambient atmosphere and the components of the system experience conductive heat transfer through the heat sink. Therefore, conduction occurs in the x, y, and z directions.

Similar to the 2D RC thermal models, the first step in designing 3D RC thermal models is to discretize the system. In the case of 3D systems, the system is discretized into voxels. Each voxel is assigned a capacitance value, again at the level of the functional element. Adjacent voxels that do not have an exposed surface to the ambient atmosphere are connected to each other through conduction resistances only. However, the voxels that are exposed to the ambient atmosphere have an additional resistance that connects them to the ambient atmosphere node in the 3D RC thermal model. The additional resistance represents the convective heat transfer from the corresponding part of the overall system to the ambient atmosphere. The conduction resistances along the x, y, and z directions are calculated using (1). However, L and A_c depend on the direction along which the heat is being conducted. In most cases, the heat sink used in power electronic systems is a finned structure. The convection resistances cannot be calculated using (2) and heat transfer equations for extended surfaces must be used (Frank et al., 2007). The effective resistance that accounts for convection in extended surfaces can be found using Frank et al. (2007)

$$R_{t,o} = \frac{1}{\eta_o h A_t}, \tag{6}$$

where $R_{t,o}$ is the overall effective resistance, η_o is the overall efficiency of an array of fins, h is the heat transfer coefficient, and A_t is the total surface area of the extended surface. The overall efficiency for an array of fins is found using Frank et al. (2007)

$$\eta_o = 1 - \frac{N A_f}{A_t}(1 - \eta_f), \tag{7}$$

where N is the number of fins in an array, A_f is the surface area of a single fin, and η_f is the efficiency of a single fin. The total surface area for N fins in an array is found using Frank et al. (2007)

$$A_t = N A_f + A_b, \tag{8}$$

where A_b is the surface area of the exposed part of the base of the extended surface. For straight rectangular fins with active tips, the efficiency of each fin in the array can be found using Frank et al. (2007)

$$\eta_f = \frac{\tanh mL_c}{mL_c}, \tag{9}$$

where L_c is a corrected length found using Frank et al. (2007)

$$L_c = L + \frac{t}{2}. \tag{10}$$

Here L is the length of the fin, and t is the thickness of the fin. If the width of a rectangular fin is much larger than its thickness, the parameter m can be found using Frank et al. (2007)

$$m = \sqrt{\frac{2h}{kt}}, \tag{11}$$

where k is the thermal conductivity of the material of the extended surface, and h is the heat transfer coefficient.

2.3. 2D Network modeling

In order to design an observer that provides an accurate dynamic spatial thermal estimation of the power electronic system, a state space representation of the thermal model is needed (Sharifi & Rosing, 2010). The state space is derived from a directed weighted graph $G = (V, E, W)$ that represents the interconnected RC thermal model, where $V = \{1, 2, \ldots, n\}$ denotes the set of nodes of a graph of n nodes, E denotes the set of edges that connect adjacent nodes, and W denotes the weights of the edges. The ambient atmosphere is modeled by a single node $(n + 1)$ with an infinite capacitance. Each node represents a capacitor in the RC model. Each directed weighted edge represents the thermal resistance between two nodes in the RC model. The direction of the edge represents the direction of positive heat flow between the corresponding adjacent nodes. The resistance values of the edges are equal in both directions, i.e. $R_{ij} = R_{ji}$ on the edge (i, j). However, since the heat can flow only in one direction (from the higher temperature node to the lower temperature node), a direction can be assigned to every edge in the graph. Fig. 3 shows the graph-based model representation of the 2-D RC thermal model of Fig. 1. The edges in Fig. 3 represent the conduction along the x and y directions between adjacent nodes in addition to convection from each node to the ambient atmosphere.

The dynamic thermal behavior is then obtained by applying conservation of energy on every node in the graph-based model. Therefore, the dynamics of the system are represented by a system of coupled first order differential equations given by

$$C_i \frac{dT_i}{dt} = q_i, \tag{12}$$

where C_i denotes the thermal capacitance of node i, T_i denotes the temperature of node i, and q_i denotes the net heat flow into node i. The heat flow into a node can be through conduction from adjacent nodes or through heat generation Q_s from the active component represented by the corresponding node. The heat flow from node i to node j is

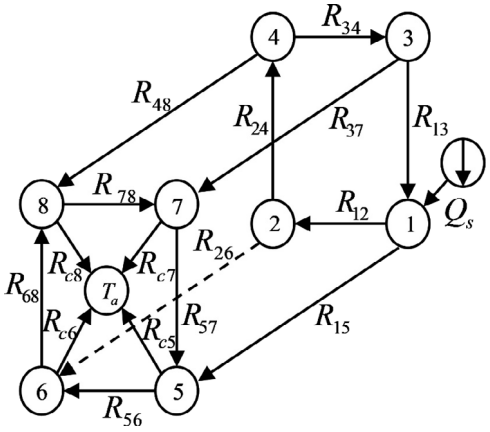

Fig. 4. Example of a 3D graph-based thermal model.

calculated as$(T_i - T_j)/R_{ij}$, where R_{ij} can be the conduction resistance or the convection resistance. The set of the coupled differential equations can be expressed in a state space form as

$$\dot{\vec{x}} = A\vec{x} + B\vec{u} + V\vec{d}, \tag{13}$$

where the state vector $\vec{x}$ represents the temperature of each node of the graph, the matrix $A = [a_{ij}]$ represents the system dynamics, the vector $\vec{u}$ represents the heat input from the heat generating components in the system, and $\vec{d}$ represents the disturbance to the system which is the ambient atmosphere in this case. The system dynamics matrix is given by

$$a_{ij} = \begin{cases} 0, & i \neq j \quad (i,j) \notin E \\ \frac{1}{C_i R_{ij}}, & i \neq j \quad (i,j) \in E \\ -\sum_{k \neq i} a_{ik} - \frac{1}{C_i R_{ci}}, & i = j \quad (i,j) \in E \end{cases} \tag{14}$$

2.4. 3D Network modeling

The state space thermal models for enclosed power electronic systems are derived from 3D RC thermal models in a manner very similar to the 2D case. However, in this case the edges of the thermal networks represent conduction in the x, y, and z directions. Fig. 4 shows an example of a 3D graph-based thermal model. The first vertical layer that contains the first 4 nodes represents the power electronic system; in this case an inverter. The current source connecting to the first node in the inverter layer represents a source of heat that exists in the corresponding location of the inverter. The second vertical layer that contains the second 4 nodes represents the heat sink. The edges in each of the two vertical layers represent conduction resistances in the x and y directions between adjacent nodes. The edges that connect the two vertical layers represent the conduction resistances in the z direction between the inverter and the heat sink. Furthermore, the layer that represents the heat sink contains additional edges connected to the ambient atmosphere node. The dynamic thermal behavior of the 3D system is then obtained using (12) which results in a system of coupled first order differential equations with a state space model structure identical to that of 2D systems.

3. Model order reduction

The reduction in system complexity is useful for on-line estimation purposes. There are many methods available in the field of model order reduction. The best known methods are Truncated Balanced Realization (Moore, 1981), Hankel-norm reduction (Glover, 1984), and Proper Orthogonal Decomposition (Schilders, 2008). For reducing the complexity of the RC thermal models studied here, a model order reduction technique that preserves the physical intuition of the original RC thermal model is needed in order to optimize sensor placement in Section 5.

The model order reduction technique used here reduces the number of nodes of the thermal model while preserving its input output behavior and the correspondence with the physical system. This technique is an aggregation based approach developed in Deng, Barooah, Mehta, and Meyn (2010). It provides a way to aggregate the nodes of the full order thermal model into single nodes, called "super-nodes", in the reduced order thermal model by applying the aggregation method of a continuous time Markov chain. The main idea behind this model order reduction technique is to find an optimal partition function $\phi : V \to M$, where $M = \{1, 2, \ldots, m\}$ with $m < n$. The partition ϕ reduces the dimension of the state space from n nodes in the full order model into m nodes in the reduced order model, where m is specified by the user. Each super-node has a super-capacitance $\bar{C}$ and a super-temperature $\bar{T}$. Super-nodes are connected by super-resistances $\bar{R}$. The super-capacitance and the super-resistance are given by

$$\bar{C}_k = \sum_{i \in V} C_i, \tag{15}$$

$$\bar{R}_{kl} = \frac{1}{\sum_{i,j \in E} \frac{1}{R_{ij}}}. \tag{16}$$

In order to aggregate the nodes of the full order model, the optimal partition function ϕ has to be found. This function is difficult to get exactly when the order of the reduced order model is greater than 2 which is the general case. Instead, the reduced order model is obtained by applying a spectral algorithm on the symmetric matrix $\bar{P} = 0.5(\Delta^{\frac{1}{2}} P \Delta^{-\frac{1}{2}} + \Delta^{-\frac{1}{2}} P^T \Delta^{\frac{1}{2}})$ for the graph-based model designed in Section 2. Here $\Delta = diag(\pi)$, where π is the stationary distribution of the Markov chain, and $P(t)$ is the Markov transition matrix. For the linear systems of interest (13), $P(t)$ is given by $P(t) := e^{At}$ (Deng, Goyal, Barooah, & Mehta, 2014). The stationary distribution is given in terms of the capacitances by

$$\pi_i = \frac{C_i}{\sum_{j \in V} C_j}, i \in v. \tag{17}$$

The spectral algorithm steps used to obtain the reduced order thermal model are shown in Table 1.

Table 1
Computation steps of the reduced order model.

Algorithm	
1.	Construct $\bar{P}$: $\bar{P} = 0.5(\Delta^{\frac{1}{2}} P \Delta^{-\frac{1}{2}} + \Delta^{-\frac{1}{2}} P^T \Delta^{\frac{1}{2}})$.
2.	Check the sign structure of the second largest eigenvector of $\bar{P}$.
3.	Aggregate the spatially adjacent nodes that share the same sign into super-nodes.
4.	Calculate the super-capacitances and super-resistances (Neglect the internal resistances in the super-nodes).
5.	Add the heat sources that exist in the same super-node into a single super-heat source.

4. Estimator design

The final step is to design an estimator that generates an accurate dynamic temperature distribution for the reduced order thermal model using the smallest possible number of sensors placed at the most efficient locations. The optimal estimator for the linear system (13) in the case of white noise is the well-known Kalman filter (Kovacevic & Durovic, 2008; Tzoumas, Jadbabaie, & Pappas, 2015; Zhang & Srivastava, 2010). A Kalman filter was designed for the linear continuous-time plant (13) and discrete-time observations given by

$$y(m) = Hx(m) + v(m) \tag{18}$$

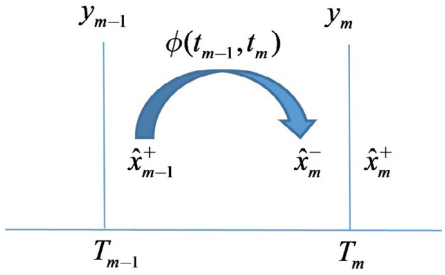

Fig. 5. Graphical illustration of the continuous–discrete Kalman filter.

where $y(m)$ is the sensors output, H is a mapping from the true states into the observed states, and $v \sim N(0, R_k)$ is the measurement noise which is assumed to be white noise with zero mean and covariance R_k. In a continuous–discrete Kalman filter, intermittent observations are easy to handle. The measurements from the temperature sensors can be taken at irregularly spaced instants of time. Another advantage of the continuous–discrete Kalman filter is that this approach provides the optimal state estimates continuously, including between the observations (Kovacevic & Durovic, 2008).

The computational cycle of the sequential estimation process of a continuous–discrete Kalman filter is shown in Fig. 5. $\hat{x}^-_m$ represents the a priori state estimate just before the latest observation $y(m)$ is received. $\hat{x}^+_{m-1}$ represents the a posteriori state estimate just after the preceding observation $y(m-1)$ is received. The a priori state estimate $\hat{x}^-_m$ is obtained by propagating the a posteriori estimate $\hat{x}^+_{m-1}$ through the state transition matrix $\phi(t_m, t_{m-1})$ according to

$$\hat{x}^-_m = \phi(t_m, t_{m-1})\hat{x}^+_{m-1}, \tag{19}$$

where the state transition matrix is given by

$$d\phi/dt = A\phi(t, \tau). \tag{20}$$

The a posteriori state estimate $\hat{x}^+_m$ is then obtained by updating the a priori state estimate $\hat{x}^-_m$ by the observations $y(m)$ according to the following recursive updating procedure

$$\hat{x}^+_m = \hat{x}^-_m + K_m(y(m) - H\hat{x}^-_m), \tag{21}$$

where K_m represents the Kalman gain matrix that results in the minimum variance estimate. K_m is given by

$$K_m = P^-_m H^T [H P^-_m H^T + R_m]^{-1}, \tag{22}$$

where the error covariance matrix P^-_m is the solution of

$$\dot{P} = AP + PA^T + Buu^T B^T. \tag{23}$$

P_0, the initial condition for P^-_m, is given by

$$P_o = E\{[x(0) - \hat{x}_0][x(0) - \hat{x}_0]^T\}, \tag{24}$$

where $\hat{x}_0 = E\{x(0)\}$. The optimized value of the updated estimation error covariance matrix is given by

$$P^+_m = [I - K_m H(m)]P^-_m. \tag{25}$$

5. Case studies

5.1. 2D case study

The thermal estimation technique developed in this article was applied to the multilevel dc–ac converter (Lei et al., 2017) shown in Fig. 6. The main components of the circuit are Gallium Nitride (GaN) gate drivers, GaN transistors, ceramic capacitors, and Adum5210 digital isolators with integrated dc-to-dc converters.

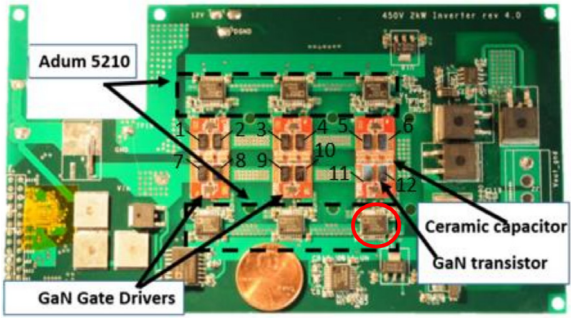

Fig. 6. Multilevel dc–ac Converter (Lei & others, 2016). The GaN transistors are labeled.

Table 2
Step loads for the 12 current sources.

Trans. #	Step load (W)	Trans. #	Step load (W)	Trans. #	Step load (W)
1	0.5	5	0.5	9	0.1
2	0.7	6	0.8	10	0.1
3	0.5	7	0.1	11	0.1
4	0.9	8	0.1	12	0.1

The main printed circuit board (PCB) is composed of four layers of copper, three layers of a glass-reinforced epoxy laminate (FR4), and two solder mask layers. The daughterboard is composed of two copper layers, one FR4 layer, and two solder mask layers. In this subsection, the heat conduction problem is solved as a 2D problem as the inverter was open to the environment. Conduction only in the x and y directions along the converter was considered. Convection takes place from the open converter to the environment. The board was divided into 39 elements, where each functional component of the board was assigned a capacitor value in the 2D RC thermal model. Since the PCB studied is multilayered, the in-plane effective thermal conductivity (4) and the effective heat capacitances (5) were used for the calculation of the R and C values of the thermal model. The board was tested for step loads in power distributed among the active elements. Table 2 illustrates the thermal power dissipated in each of the 12 transistors labeled in Fig. 6 and represented as current sources (i.e. heat sources) in the thermal network. The resulting 39 state thermal model was aggregated into 9 "super-nodes". Fig. 7 shows the network of the 39 state full order model and the 9 super-nodes of the aggregated model. The reduced order model had an error of less than 3 ° C with respect to the full order model. Fig. 8 shows the error between the fifth (tr_5) and sixth (tr_6) states of the reduced order model and their equivalent states of the full order model. The full order model states are represented by solid lines and the reduced order model states are represented by circles.

Infrared (IR) thermal video was used for experimental validation using a FLIR T420 IR camera. Fig. 9 represents a snapshot from the thermal video at 2 min and 58 s after the voltage was applied to the converter. The temperature scale is in °C. Fig. 10 shows theoretical vs experimental results of the fifth and sixth states of the reduced order model. These states represent the most critical spots on the board where temperature needs to be monitored carefully. They represent the dynamic thermal behavior of the highest temperature components on the board (i.e. GaN transistors, GaN gate drivers, and ceramic capacitors). It should be noted that heat sources in super-nodes 3, 4, and 5 are almost generating the same amount of heat as shown in Table 2. Hence, the remaining GaN transistors and GaN gate drivers operating at high temperature (i.e. super-nodes 3 and 4) should have similar thermal dynamics as super-node 5. Experimental results are within an error of +/− 5 ° C. The remaining states were not shown for brevity but the interested reader is referred to (Tannous, 2017) for validation of all states.

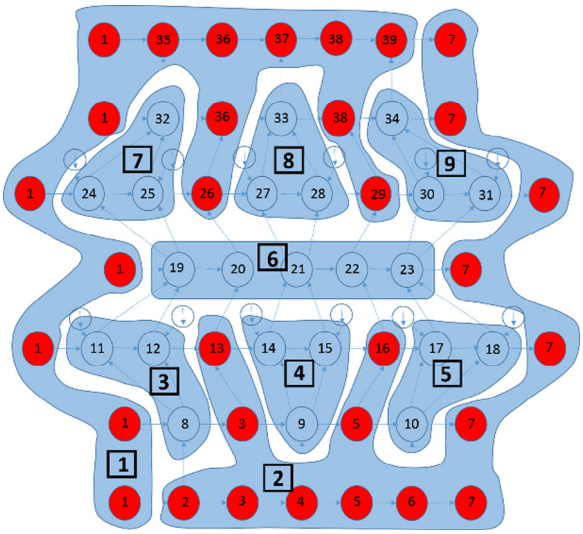

Fig. 7. Directed weighted graph representing the interconnected RC thermal model of the full order model and the reduced order model.

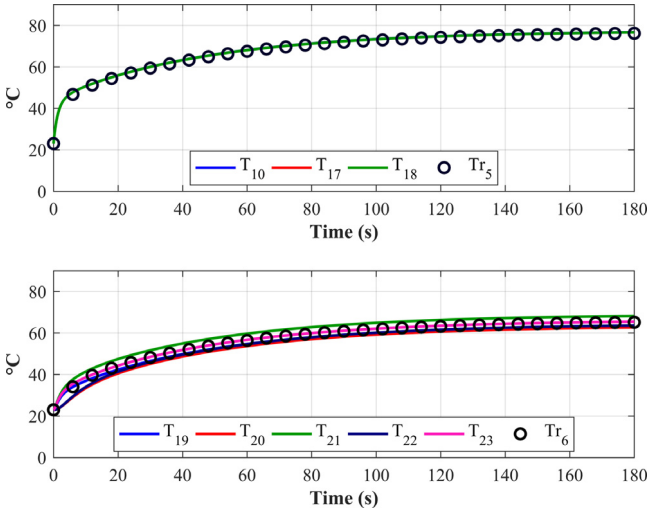

Fig. 8. Simulation of fifth and sixth state of the reduced order model vs equivalent states of the full order model.

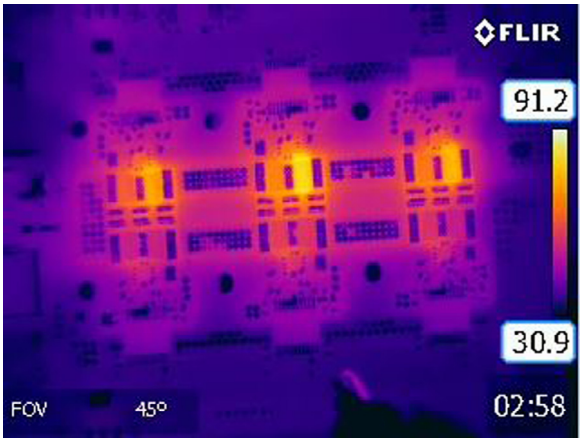

Fig. 9. Snapshot from IR Measurement of Operating Multilevel Inverter.

Once an accurate reduced order model was developed, an optimization procedure was performed with respect to the number and placement of temperature sensors. The optimization formulation was done with the underlying assumption that there can be a maximum of 1 sensor per state since these are connections of first order systems. It means that a particular state may either have a sensor or not.

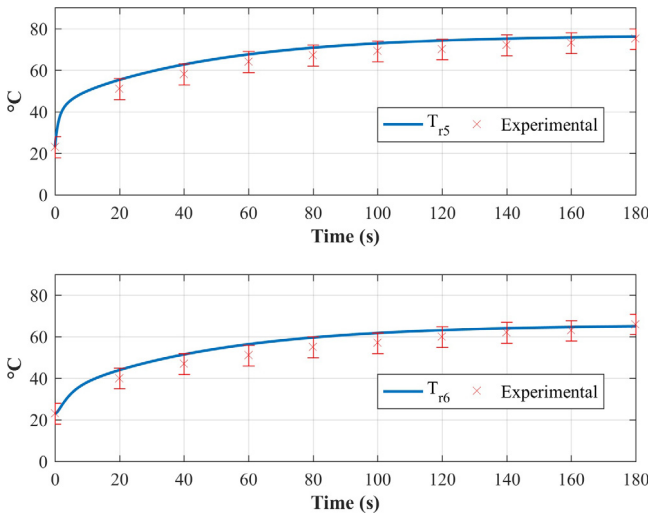

Fig. 10. Simulated theoretical results (RC model) vs experimental results (IR thermal video) of the fifth and sixth states of the reduced order model.

Sensors can be placed based on the degree of observability of the states. There are many such metrics by which one can determine the degree of observability of the states of a dynamic system (Brewer, Huang, Singh, Misra, & Hahn, 2007; Singh & Hahn, 2005a,b). The trace analysis of the observability Gramian (Samad, Siegel, Stefanopoulou, & Knobloch, 2015; Zanini, Atienza, & De Micheli, 2013) has been considered as the performance metric for optimal sensor placement here. The larger the trace of the observability Gramian, the greater the observability. There are 2^9 and 2^{39} combinations in which the temperature sensors can be placed for the reduced order model and full order model, respectively. The sensor placement optimization has been performed using mixed integer linear programming (MILP) genetic algorithm (GA). The sensor placement optimization problem has a discontinuous objective function and both integer and continuous design variables. MILP GA can directly handle problems of this nature and, as such, is a good candidate for use. Gradient based algorithms (Akbarzadeh, Levesque, Gagne, & Parizeau, 2014) may also be used to solve this problem with modifications to handle the MILP through continuous relaxation (Joshi & Boyd, 2009) of integer design variables. The GA was chosen because it can efficiently handle the MILP, albeit with steps taken to avoid local minima. That said, the general approach allows us to substitute different optimization routines at the preference of the user.

As the number of sensors increases, the trace of the observability Gramian increases. Hence, there exists a trade-off between the degree of observability and the number of sensors that can be placed on the converter. The optimal number of sensors was found by analyzing the state estimation error with respect to the number of sensors used in the Kalman filter. Fig. 11 shows the sum of root mean square error (rmse) of the states of the 2D reduced order thermal model with respect to the number of sensors used. For each number of sensors used, the sensors were placed at the optimal locations obtained by maximizing the trace of the observability Gramian. The sum of rmse decreased by increasing the number of sensors in the system and encountered a noise floor after using 5 sensors in the Kalman filter. The noise on the sensors removed ability to gain additional information even with additional sensors. Therefore, the optimal number of temperature sensors was determined to be 5 sensors.

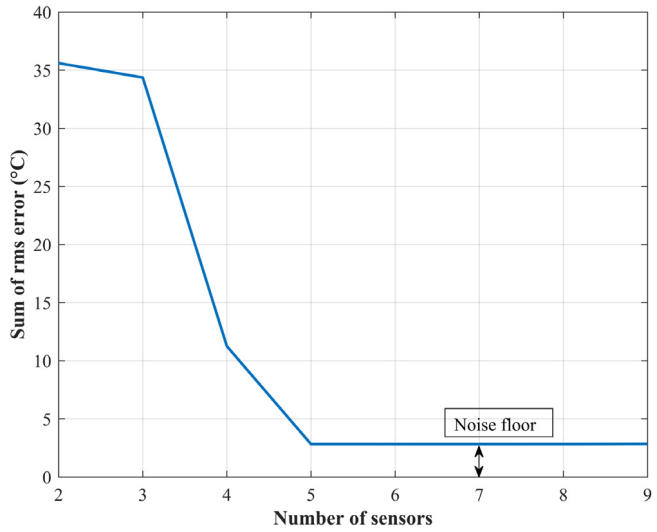

Fig. 11. Sum of rmse of the states of the 2D reduced order model as a function of the number of sensors.

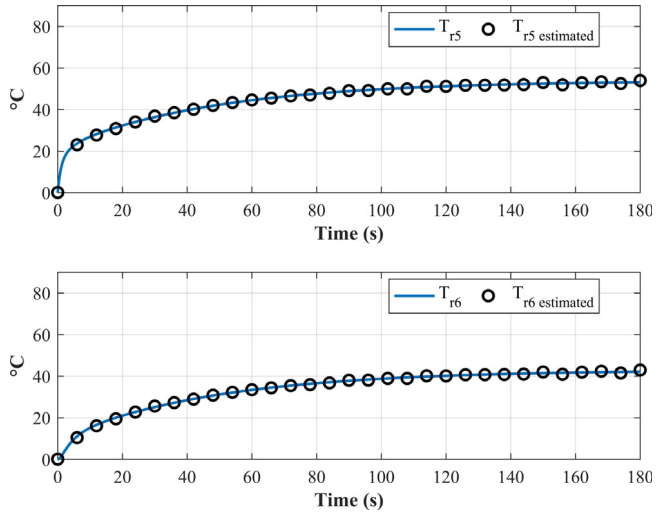

Fig. 12. Theoretical (RC model) vs estimated (Kalman filter) values of the fifth and sixth states of the reduced order model; simulation results.

The optimal locations of the 5 sensors, according to the trace of observability Gramian, were on super-nodes 1, 2, 5, 6, and 7. A continuous–discrete Kalman filter was designed for the reduced order model and Fig. 12 shows the simulated theoretical versus the estimated values of the fifth and sixth states of the reduced order model, respectively. The states of the full order model were also estimated by applying a reduced order Kalman filter on the full order model. Since there is a small error between the states of the full order model and the states of the reduced order model, the estimated values of the states of the full order model were slightly different than the theoretical values of these states. However, the estimation errors were still less than 3 ° C. Fig. 13 shows the simulated estimated values of the fifth and sixth states of the reduced order model obtained from the Kalman filter versus their corresponding theoretical equivalent states in the full order model obtained from the full order RC model.

5.2. 3D case study

To further test the approach in a more realistic environment, the estimation method was also applied to an inverter board that was

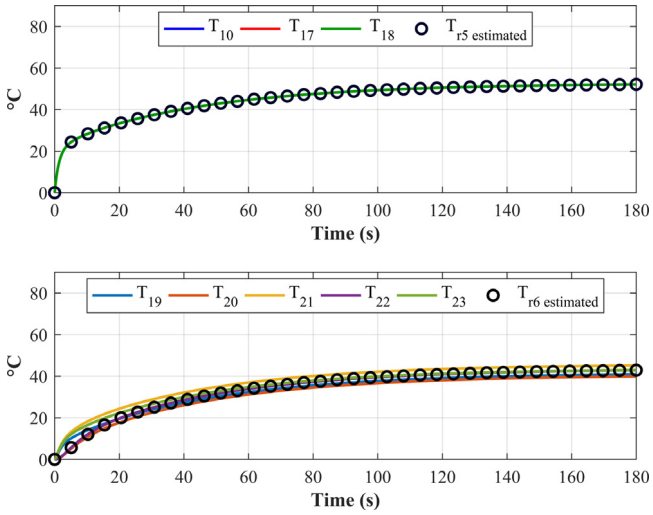

Fig. 13. Estimated values of the fifth and sixth states of the reduced order model (Kalman filter) vs their corresponding theoretical equivalent states in the full order model (RC model); simulation results.

enclosed with a heat sink attached. The inverter with a heat sink is shown in Fig. 14 where the heat sink is made of aluminum. A 0.02" fiberglass-reinforced filler and polymer thermal gap pad (Gap Pad 5000S35) was placed on top of the active components to fill the air gaps between the active components of the inverter and the base of the aluminum heat sink.

Similar to the 2D case, discretization was made at the level of the functional elements. The discretization of the inverter board did not change, resulting in the same 39 capacitors as before. The thermal capacitance of the thermal gap pads was neglected. The heat sink was discretized into 39 nodes that have the same locations as the nodes of the inverter. Therefore, the full order RC thermal model resulted in 78 capacitors: 39 capacitors for the inverter and 39 capacitors for the heat sink. The 3D RC thermal model accounts for conduction along the x and y directions in the inverter, conduction in the z direction from each node of the inverter to the corresponding node in the heat sink, conduction along the x and y directions in the heat sink, and convection from each node of the heat sink to the environment. It should be noted that the additional thermal resistance of the thermal gap pads was included in the conduction resistance in the z direction from the inverter to the aluminum heat sink.

The main heat sources in the enclosed inverter are still the GaN transistors. Therefore, the 3D RC thermal model had 12 current sources that represent the 12 GaN transistors used in the board. The power cycle for each current source is shown in Fig. 15. These loads represent thermal losses from each of the 12 GaN transistors (i.e. the 98% efficient board is operating at 15 W). A lower value than the previous 2D case study was used in order to demonstrate the sensitivity of this approach.

The 78 states of the full order 3D RC thermal model are shown in Fig. 16. The temperature shown in Fig. 16 is the relative temperature with respect to the ambient temperature. The hottest spot in the system experienced a temperature increase of 5 ° C above the ambient temperature. Since the system is enclosed, IR thermal imaging is not a candidate validation tool. Instead, 13 thermocouples were placed at various locations on the board and affixed with Kapton tape.

The thermal network of the inverter layer in the 3D system is the same as the 2D system. Hence, applying the model order reduction method on the inverter in the 3D system resulted in the same 9 super-nodes of the 2D reduced order model. The homogeneity of the material of the heat sink allowed an even distribution of the heat along the base of the heat sink. The conduction resistances in the x and y directions in the heat sink were determined to be negligible relative to others in

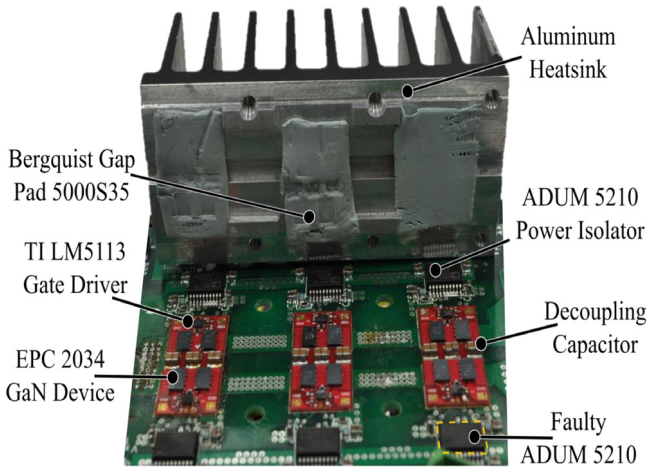

Fig. 14. Multilevel dc–ac converter enclosed with a heat sink. The heat sink is made of aluminum. A thermal gap pad (Gap Pad 5000S35) was placed on top of the active components.

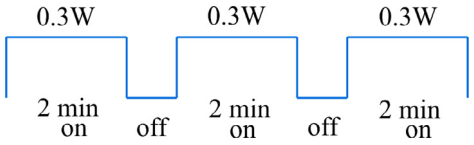

Fig. 15. Thermal power cycle for the 12 current sources of the 3D RC thermal model.

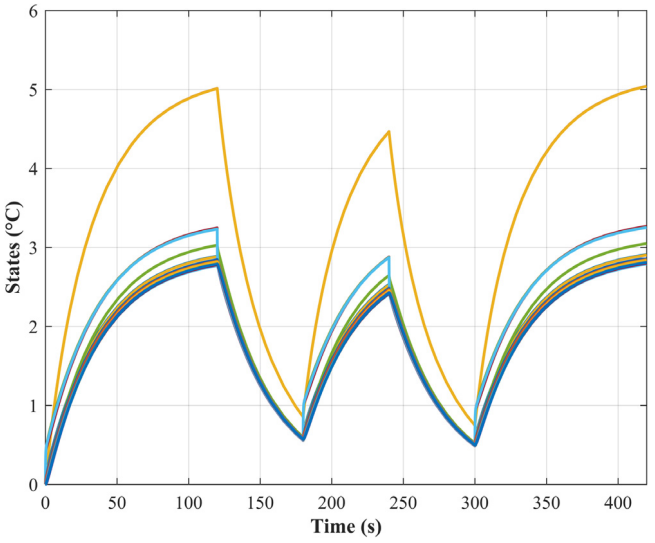

Fig. 16. Simulation of the 78 states of the full order 3D RC thermal model (39 states for the inverter and 39 states for the heat sink).

the system. Therefore, the 39 nodes of the heat sink were aggregated into a single super-node. The overall 3D reduced order RC thermal model resulted in 9 super-nodes for the inverter and 1 super-node for the heat sink. These 10 states were estimated using a Kalman filter. The optimal locations of the thermocouples were again found by maximizing the trace of the observability Gramian. The optimal number of thermocouples was found based on the error between the actual temperature of the board and the estimated temperature of the board obtained from the Kalman filter. Fig. 17 represents the sum of rmse of the 10 states of the 3D reduced order model as a function of number of sensors used in the Kalman filter. The sum of rmse decreased by adding sensors in the system and approached the noise floor limit after using 9 sensors. However, as it can be seen in Fig. 17, the decrease in the sum

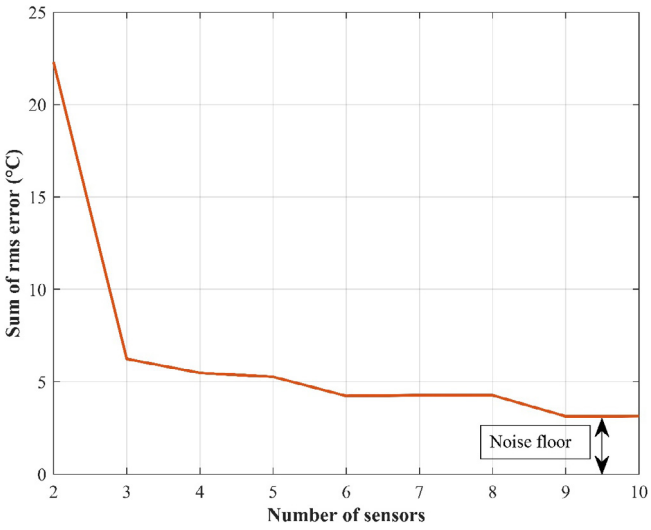

Fig. 17. Sum of rmse of the states of the 3D reduced order thermal model vs number of sensors used.

of rmse is minimal after using 6 sensors (i.e. there is a minimal improve in estimation accuracy by using more than 6 sensors). Therefore, the optimal number of sensors was determined to be 6 sensors for this case. Hence, the dynamic thermal model (i.e. RC model) of the inverter was validated experimentally by placing 13 sensors at different locations on the board. However, the Kalman filter used only a subset of six sensors placed at optimal locations on the board in order to estimate the dynamic thermal behavior of the inverter. The sensors were placed on super-nodes 1, 2, 4, 6, 8, and 10. The nominal estimation performance of the 3D system is similar to the 2D system in terms of accuracy and not repeated for this case study.

We now demonstrate the utility of the approach as a fault diagnostic tool. To detect a fault, the actual dynamic thermal behavior of the system is compared to the estimated dynamic thermal behavior obtained from the reduced order Kalman filter. A significant difference (i.e. above a certain threshold) between these two behaviors reflects the existence of a faulty component in the system. To isolate the fault (i.e. to locate the faulty component in the system), an additional heat source input is injected to one of the super-nodes of the reduced order thermal model and actual and estimated behaviors are compared again. If there is a match between the two behaviors, the faulty component is the one represented by the super-node with the additional heat source. If there is a mismatch between the two behaviors, then the additional heat source should be moved to another super-node and the process should be repeated. Automated fault detection and isolation algorithms (Gao, Cecati, & Ding, 2015; Hwang, Kim, Kim, & Seah, 2010) are valuable but outside the scope of this work. In the current work, the localization of the faulty component is a manual process where additional inputs are injected sequentially at each node to determine which node contains the fault. The fault detection and isolation algorithm used in this work is represented in Fig. 18.

To demonstrate this approach on the inverter board, an intentionally faulty component, represented by a heat source with a ramped power profile is inserted into the system at the location marked with a red circle in Fig. 6. The experimental readings of the 13 sensors shown in Fig. 19 illustrates a resulting steady drift in system measurements. We first consider the states of the full order model shown in Fig. 16. A residual generated by the difference between Figs. 16 and 19 would eventually exceed a threshold indicating a serious fault, i.e. a failing component that was overheating.

The location of the failing component can be discovered by considering the estimated states of the reduced order RC thermal model obtained

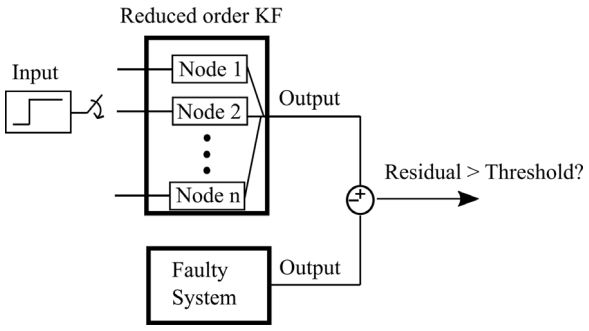

Fig. 18. Fault detection and isolation algorithm.

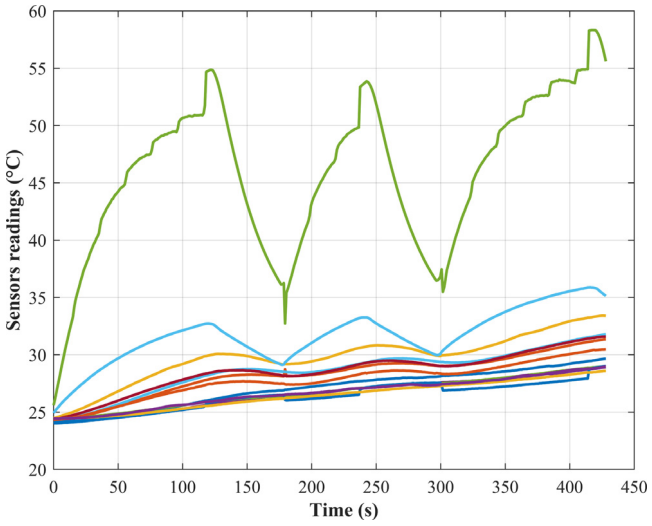

Fig. 19. The measurements of the 13 sensors.

from the Kalman filter. The ramped heat source was connected to super-node 2 in the reduced order RC thermal model replicating the failing component. Fig. 20 shows a comparison between the experimentally measured data and the estimated states for super-nodes 5 and 9 of the reduced order RC thermal model that includes the additional heat source. Other states performed similarly. Hence, the failing component can be isolated to the particular super-node (i.e. super-node 2) with high confidence. In practice, the fault signal may have to be applied to multiple super-nodes to isolate the problem but this is far more tractable than trying individual nodes for the full order model.

6. Conclusion

Accurate state estimates are essential for dynamic thermal management techniques in high power density systems. This paper provides an approach for temperature estimation and fault detection in complex and interconnected thermal systems. The dynamic spatial temperature profile of lumped parameter models was accurately reconstructed using an optimal estimator together with an optimal number and placement of temperature sensors. A structure-preserving model order reduction technique based on Markov chain aggregation was used to reduce the complexity of the thermal model. The proposed method was applied on a 2D system in which an inverter was open to the ambient temperature. Furthermore, the proposed method was applied on a 3D system in which the inverter was enclosed with a heat sink in order to increase the heat transfer from the system to the ambient atmosphere. The dynamic thermal behavior of both systems was accurately reconstructed using a small number of thermocouples. Also, it was shown how the proposed method can be used for fault detection and isolation.

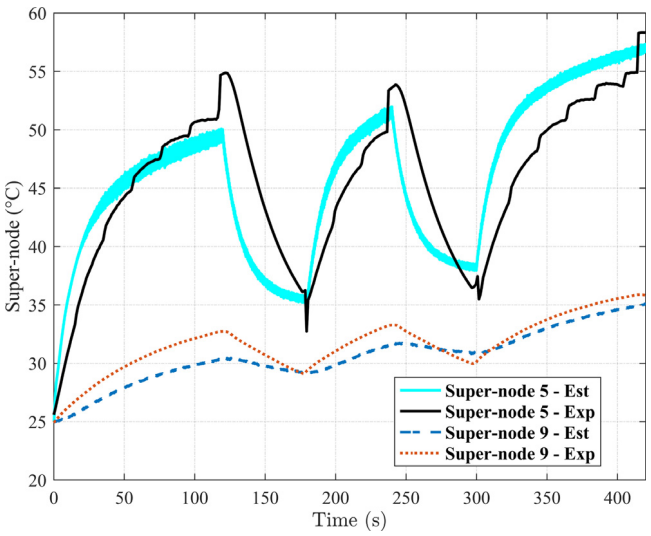

Fig. 20. Actual measured data vs estimated states for super-nodes 5 and 9 of the reduced order RC thermal model that includes the intentional additional heat source.

Conflict of interest

The authors declare that they have no conflict of interest.

Funding

This material is based upon work supported by the National Science Foundation Engineering Research Center for Power Optimization of Electro-Thermal Systems (POETS), United States with cooperative agreement EEC-1449548.

References

Akbarzadeh, V., Levesque, J.-C., Gagne, C., & Parizeau, M. (2014). Efficient sensor placement optimization using gradient descent and probabilistic coverage. *Sensors*, *14*(8), 15525–15552.

Atherton, D. P. (1982). *Nonlinear control engineering*. Van Nostrand Reinhold.

Brewer, J., Huang, Z., Singh, A. K., Misra, M., & Hahn, J. (2007). Sensor network design via observability analysis and principal component analysis. *Industrial and Engineering Chemistry Research*, *46*, 8026–8032.

Coskun, A. K., Rosing, T. S., & Whisnant, K. (2007). Temperature aware task scheduling in MPSoCs. In *Proceedings -design, automation and test in Europe*.

Davidson, J. N., Stone, D. A., Foster, M. P., & Gladwin, D. T. (2016). Real-Time temperature estimation in a multiple device power electronics system subject to dynamic cooling. *IEEE Transactions on Power Electronics*, *31*(4), 2709–2719.

Deng, K., Barooah, P., Mehta, P. G., & Meyn, S. P. (2010). *Building thermal model reduction via aggregation of states*. American Control Conference, ACC.

Deng, K., Goyal, S., Barooah, P., & Mehta, P. G. (2014). Structure-preserving model reduction of nonlinear building thermal models. *Automatica*, *50*(4), 1188–1195.

Frank, A. S. L., Incropera, P., DeWitt, David P., & Bergman, Theodore L. (2007). *Fundamentals of heat and mass transfer* (6th ed.).

Gao, Z., Cecati, C., & Ding, S. X. (2015). A survey of fault diagnosis and fault-tolerant techniques part I: Fault diagnosis. *IEEE Transactions on Industrial Electronics*, *62*(6), 3768–3774.

Glover, K. (1984). All optimal Hankel-norm approximations of linear multivariable systems and their L, ∞ -error bounds. *International Journal of Control*, *39*(6), 1115–1193.

Huang, W., Ghosh, S., Velusamy, S., Sankaranarayanan, K., Skadron, K., & Stan, M. R. (2006). HotSpot: A compact thermal modeling methodology for early-stage VLSI design. *IEEE Transactions Very Large Scale Integrated System*, *14*(5), 501–513.

Hwang, I., Kim, S., Kim, Y., & Seah, C. E. (2010). A survey of fault detection, isolation, and reconfiguration methods. *IEEE Transactions Control System Technology*, *18*(3), 636–653.

Iachello, M., et al. (2014). Lumped Parameter modeling for thermal characterization of high-power modules. *IEEE Transactions Components, Packaging, and Manufacturing Technology*, *4*(10), 1613–1623.

Jena, C., Sarbhai, N., Mulaveesala, R., & Tuli, S. (2006). Pulsed thermography simulation : 1D, 2D and 3D Electro-Thermal model based evaluation. In *Proc. national seminar on non-destructive evaluation*.

Joshi, S., & Boyd, S. (2009). Sensor selection via convex optimization. *IEEE Transactions on Signal Processing*, *57*(2), 451–462.

Kovacevic, P. D. B., & Durovic, P. D. Z. (2008). *Fundamentals of stochastic signals, systems and estimation theory with worked examples*. 2nd ed..

Lei, Y., et al. (2016). A 2 kW, Single-Phase, 7-Level, GaN inverter with an active energy buffer achieving 216 W/in∧3 Power Density and 97.6% peak efficiency. *Applied power electronics conference and exposition - APEC*.

Lei, Y., et al. (2017). A 2 kW, Single-Phase, 7-Level flying capacitor multilevel inverter with an active energy buffer. *IEEE Transactions on Power Electronics*, *32*(11), 8570–8581.

Lim, C. H., Daasch, W. R., & Cai, G. (2002). A thermal-aware superscalar microprocessor. In *Proceedings - international symposium on quality electronic design, ISQED*.

Moore, B. (1981). Principal component analysis in linear systems: Controllability, observability, and model reduction. *IEEE Transactions Automation Control*, *26*(1), 17–32.

Pedram, M., & Nazarian, S. (2006). Thermal modeling, analysis, and management in VLSI circuits: Principles and methods. *Proceedings of the IEEE*, *94*(8), 1487–1501.

Samad, N. A., Siegel, J. B., Stefanopoulou, A. G., & Knobloch, A. (2015). Observability analysis for surface sensor location in encased battery cells. In *Proceedings of the American control conference, ACC*.

Schilders, W. (2008). Introduction to model order reduction.

Sharifi, S., Liu, C. C., & Rosing, T. S. (2008). Accurate temperature estimation for efficient thermal management. In *Proceedings of the 9th international symposium on quality electronic design, ISQED*.

Sharifi, S., & Rosing, T. S. (2010). Accurate direct and indirect on-chip temperature sensing for efficient dynamic thermal management. *IEEE Transactions on Computer-Aided Design of Integrated Circuits and Systems*, *29*(10), 1586–1599.

Singh, A. K., & Hahn, J. (2005a). Determining optimal sensor locations for state and parameter estimation for stable nonlinear systems. *Industrial and Engineering Chemistry Research*, *44*(15), 5645–5659.

Singh, A. K., & Hahn, J. (2005b). *On the use of empirical gramians for controllability and observability analysis*. American Control Conference, ACC.

Skadron, K., Abdelzaher, T., & Stan, M. R. (2002). Control-theoretic techniques and thermal-RC modeling for accurate and localized dynamic thermal management. In *Proc. Eighth Int. Symp. High Perform. Comput. Archit.*.

Swift, G., Molinski, T. S., & Lehn, W. (2001). A fundamental approach to transformer thermal modeling - Part I: Theory and equivalent circuit. *IEEE Transactions on Power Delivery*, *16*(2), 171–175.

Tannous, P. J. (2017). Dynamic temperature estimation of power electronics systems. M.S. thesis, University of Illinois at Urbana-Champaign.

Tzoumas, V., Jadbabaie, A., & Pappas, G. J. (2015). *Sensor placement for optimal Kalman filtering: Fundamental limits, submodularity, and algorithms*. American Control Conference, ACC.

Zanini, F., Atienza, D., & De Micheli, G. (2013). A combined sensor placement and convex optimization approach for thermal management in 3D-MPSoC with liquid cooling. *Integration, The VLSI Journal*, *46*(1), 33–43.

Zanini, F., Atienza, D., Jones, C. N., & De Micheli, G. (2010). Temperature sensor placement in thermal management systems for MPSoCs. In *Circuits and systems, ISCAS, proceedings of IEEE international symposium on*.

Zhang, Y., & Srivastava, A. (2010). Adaptive and autonomous thermal tracking for high performance computing systems. *Proc. 47th Des. Autom. Conf.* - DAC '10, 68.

Zhang, Y., Srivastava, A., & Zahran, M. (2008). Chip level thermal profile estimation using On-chip temperature sensors. In *IEEE international conference on computer design, ICCD*.